Supplementary information (ESI) for Journal of Materials Chemistry

A Robust Flame Retardant Fluorinated Polyimide Nanofiber Separator for High-Temperature Lithium-Sulfur Batteries

Xiang Luo,[†a,b] Xianbo Lu,[†c] Xiaodong Chen,[†*a,b] Ya Chen,[d] Chunyu Song,[a] Chunyang Yu,[e] Nannan Wang,[a] Dawei Su,[b] Chengyin Wang,[f] Xiaochun Gao,*[b] Guoxiu Wang*[b] and Lifeng Cui*[a]

[a] School of Materials Science and Engineering, Dongguan University of Technology, Dongguan 523808, P. R. China.

[b] Center for Clean Energy Technology, School of Mathematical and Physical Science, Faculty of Science, University of Technology Sydney, NSW 2007, Australia.

[c] R&D Center, Shanghai Kingfa Sci. & Tech. Co., Ltd., Shanghai 201714, P. R. China.

[d] School of Physical Science and Technology, ShanghaiTech University, Shanghai 201210, P. R. China.

[e] School of Chemistry & Chemical Engineering, Shanghai Key Laboratory of Electrical Insulation and Thermal Aging, State Key Laboratory of Metal Matrix Composites Shanghai Jiao Tong University,Shanghai 200240, P. R. China

[f] College of Chemistry and Chemical Engineering, Yangzhou University, Yangzhou 225002, China

† These authors contributed equally to this work.

*Corresponding authors.
Emails: chenxd@dgut.edu.cn; xiaochun.gao@student.uts.edu.au; Guoxiu.Wang@uts.edu.au; lcui@dgut.edu.cn

Electronic Supplementary Information

Figure captions:

Fig. S1. Photographs of F/PI separator: (a) initial, (b) immersed in electrolyte, (c) twice dried in the oven.

Fig. S2. SEM images of (a) PI nanofiber membrane and (b) Celgard separator.

Fig. S3. (a) Electrolyte uptake, (b) electrolyte retention of F/PI, PI and Celgard separators.

Fig. S4. Electrolyte contact angles of F/PI, PI and Celgard separators.

Fig. S5. (a) DSC, (b) TGA curves of F/PI, PI and Celgard separators.

Fig. S6. Photographs of polysulfide permeation across the F/PI, PI and Celgard separators for standing times of 0 h, 5 h, 10 h, 15 h and 20 h respectively.

Fig. S7 UV-vis spectra of polysulfide solutions after 10 h, indicating the superior performance of F/PI separator.

Fig. S8. (a) Chronoamperometry profiles and (b) impedance plots estimating the Li^+ conductivity for different separators.

Fig. S9. The first five cycles' CV curves (a - c), the CV curves at various voltage scan rates (d - f), as well as the corresponding linear fits of the peak currents (g - i) of Li-S batteries with F/PI, PI and Celgard separators, respectively.

Fig. S10. The relationship between Z' and $\omega^{-1/2}$ in the low frequency region of batteries with different separators.

Fig. S11. Cycle performance of the batteries assembled with F/PI, PI and Celgard separators at 0.1C.

Fig. S12. (a) Rate capability and (b-e) discharge-charge profiles of the battery assembled by F/PI separators with E/S (electrolyte/sulfur, unit: μL/mg) ratio of 5, 15, 35, and 75, respectively.

Fig. S13. XPS of F 1s peaks for PI separator after cycling tests.

Fig. S14. SEM for (a) F/PI and (b) PI nanofiber membrane after discharge-charge for 200 cycles.

Fig. S15 SEM images of the lithium anode (a) before and after rate performance with (b) F/PI and (c) Celgard separators, respectively. The corresponding elemental mappings of sulfur in the

lithium anode with (d) F/PI and (e) Celgard separators after the rate tests, respectively. The corresponding elemental mappings of sulfur in cathode with (f) F/PI and (g) Celgard separators after the rate tests.

Fig. S16. Comparison of the cycling stability of Li plating/stripping stability with different separators at a current density of 2 mA cm^{-2} with a capacity limitation of 1 mA h cm^{-2}.

Fig. S17. Average thermograms of F/PI, PI, and Celgard separators.

Fig. S18. Photographs comparison of polysulfide diffusion through the F/PI, PI and Celgard separators at 60°C.

Fig. S19. Cycling performance of F/PI, PI, and Celgard-based batteries with higher sulfur loading at room temperature and high temperature (60°C).

Fig. S20. (a) XRD patterns, (b) FT-IR spectra, (c, d) SEM images of F/PI separators after cycling performance at 60°C.

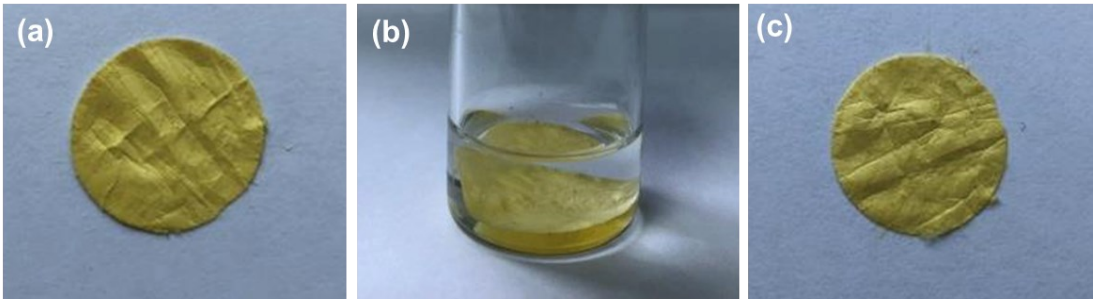

Fig. S1. Photographs of F/PI separator: (a) initial, (b) immersed in electrolyte, (c) twice dried in the oven.

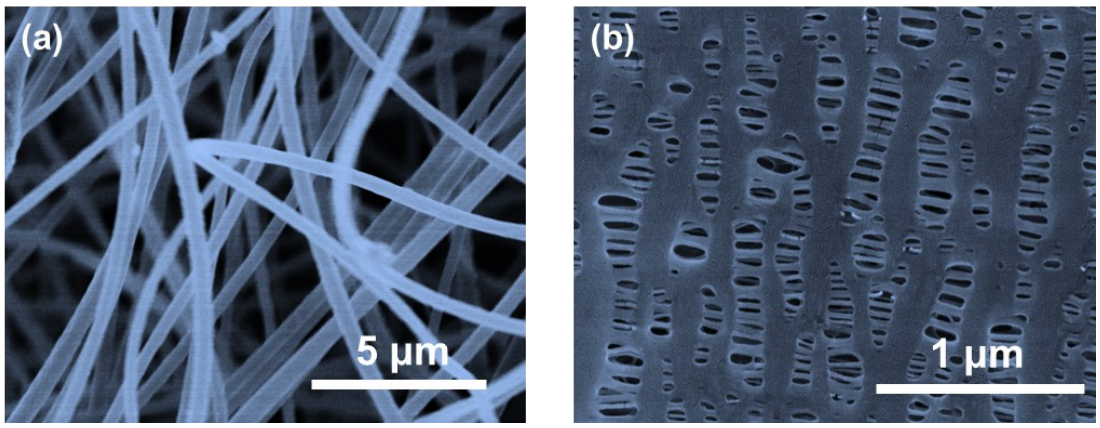

Fig. S2. SEM images of (a) PI nanofiber membrane and (b) Celgard separator.

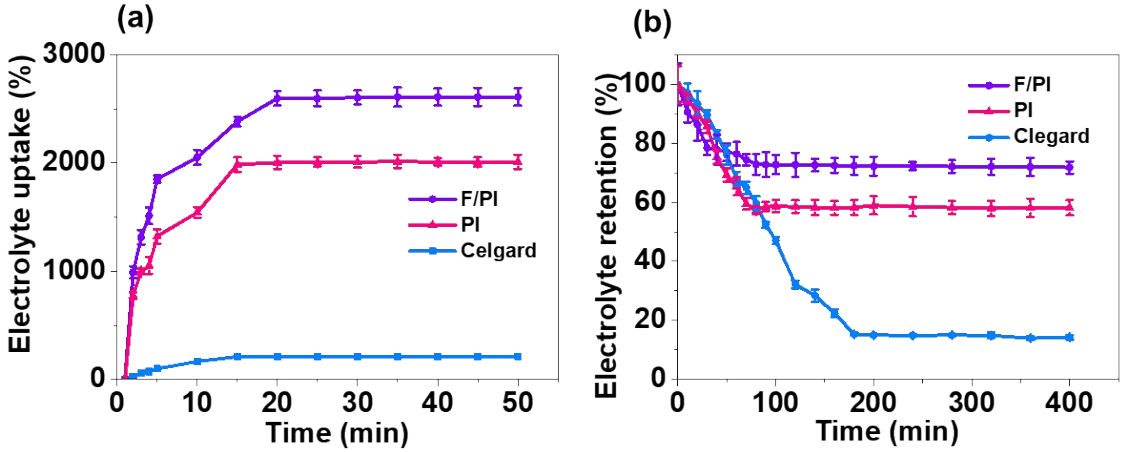

Fig. S3. (a) Electrolyte uptake, (b) electrolyte retention of F/PI, PI and Celgard separators.

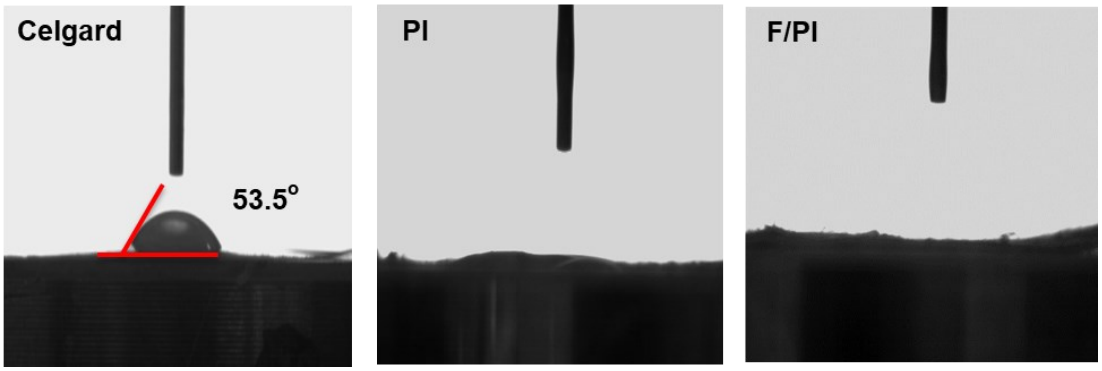

Fig. S4. Electrolyte contact angles of F/PI, PI and Celgard separators.

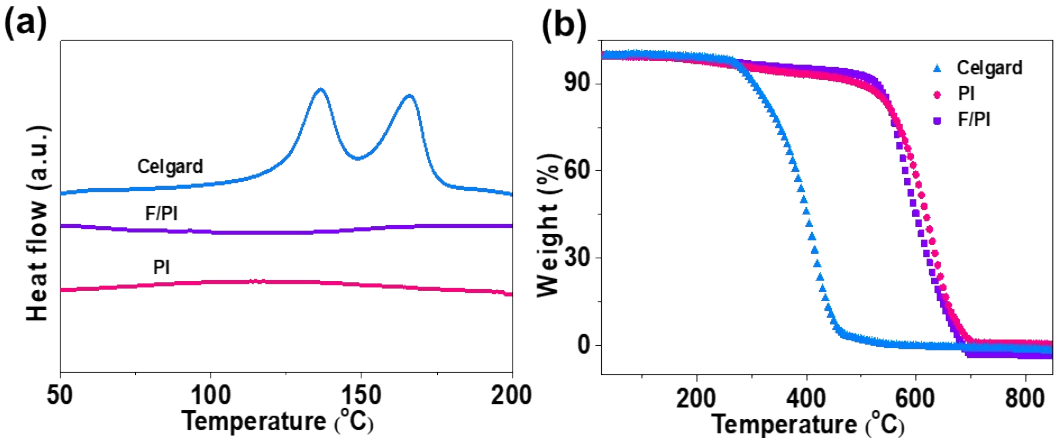

Fig. S5. (a) DSC, (b) TGA curves of F/PI, PI and Celgard separators.

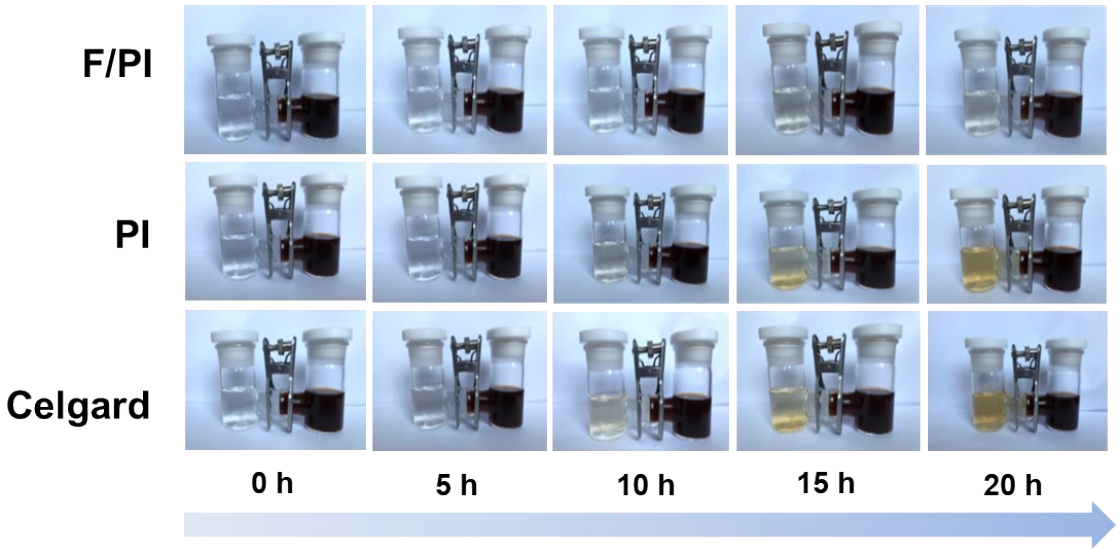

Fig. S6. Photographs of polysulfide permeation across the F/PI, PI and Celgard separators for standing times of 0 h, 5 h, 10 h, 15 h and 20 h respectively.

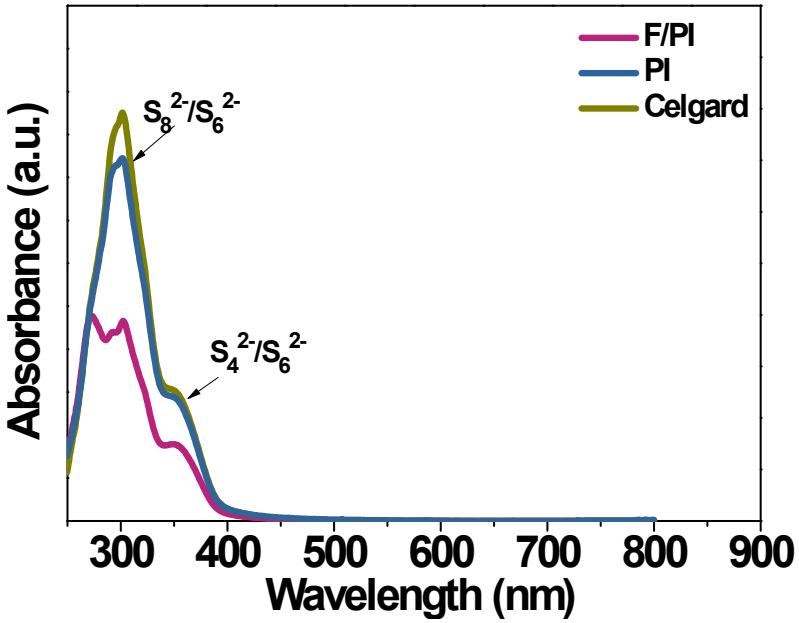

Fig. S7. UV-vis spectra of polysulfide solutions after 10 h, indicating the superior performance of F/PI separator.

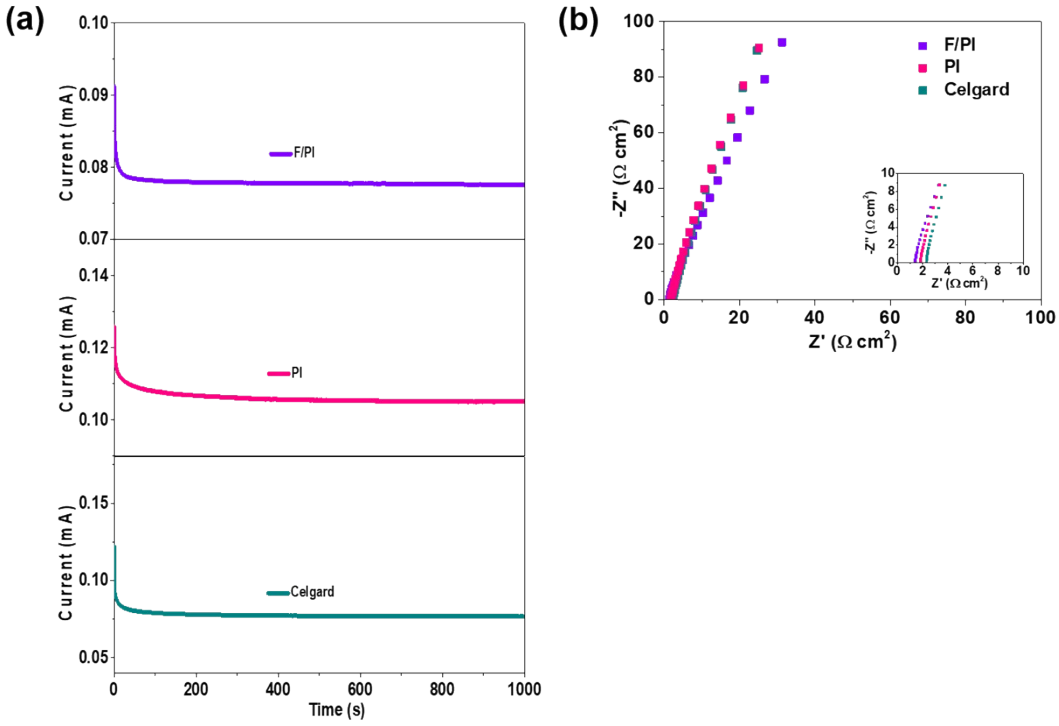

Fig. S8. (a) Chronoamperometry profiles and (b) impedance plots estimating the Li^+ conductivity for different separators.

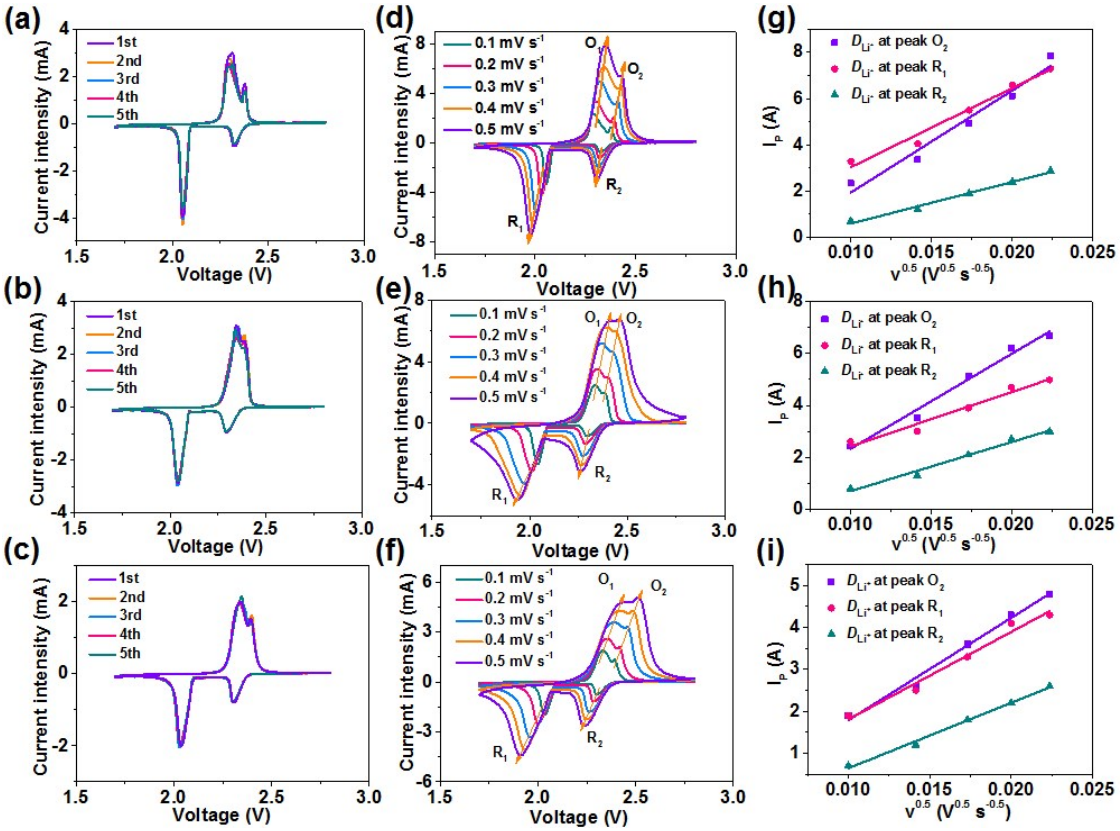

Fig. S9. The first five cycles' CV curves (a - c), the CV curves at various voltage scan rates (d - f), as well as the corresponding linear fits of the peak currents (g - i) of Li-S batteries with F/PI, PI and Celgard separators, respectively.

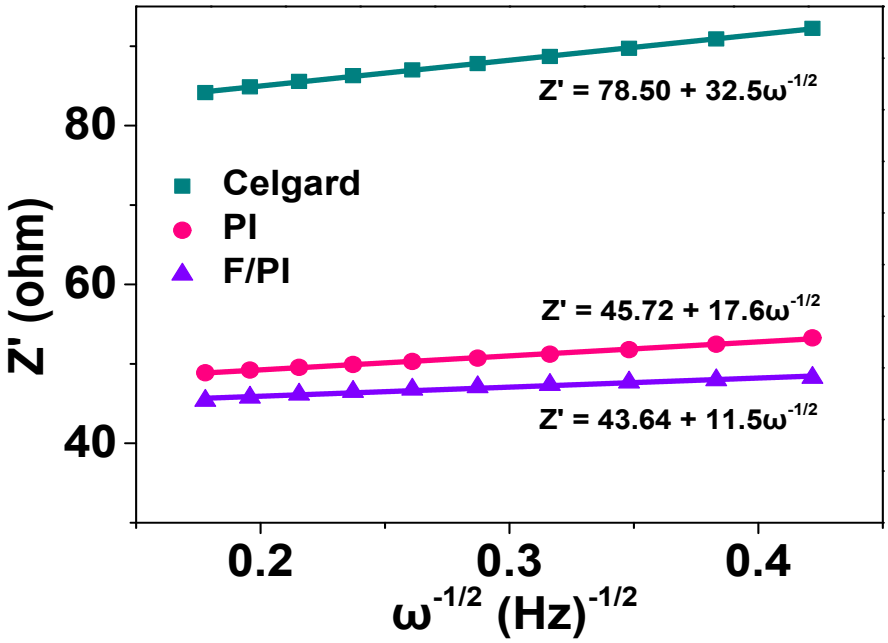

Fig. S10. The relationship between Z′ and $\omega^{-1/2}$ in the low frequency region of batteries with different separators.

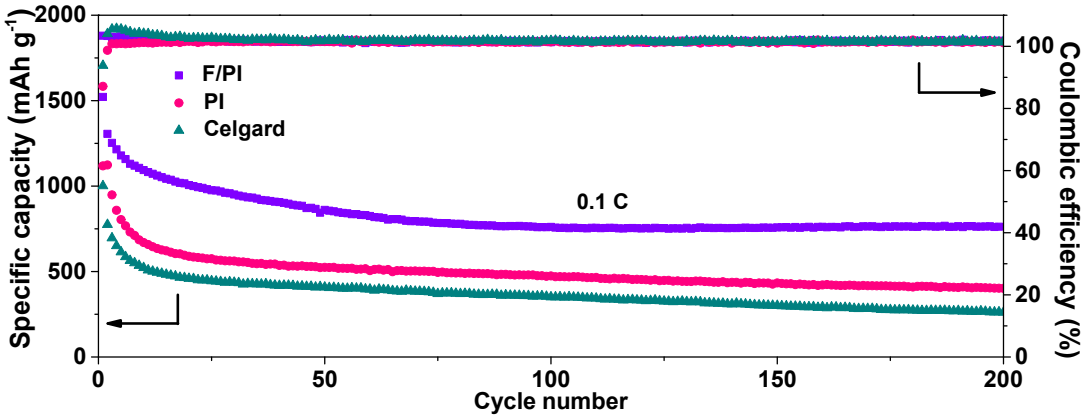

Fig. S11. Cycle performance of the batteries assembled with F/PI, PI and Celgard separators at 0.1C.

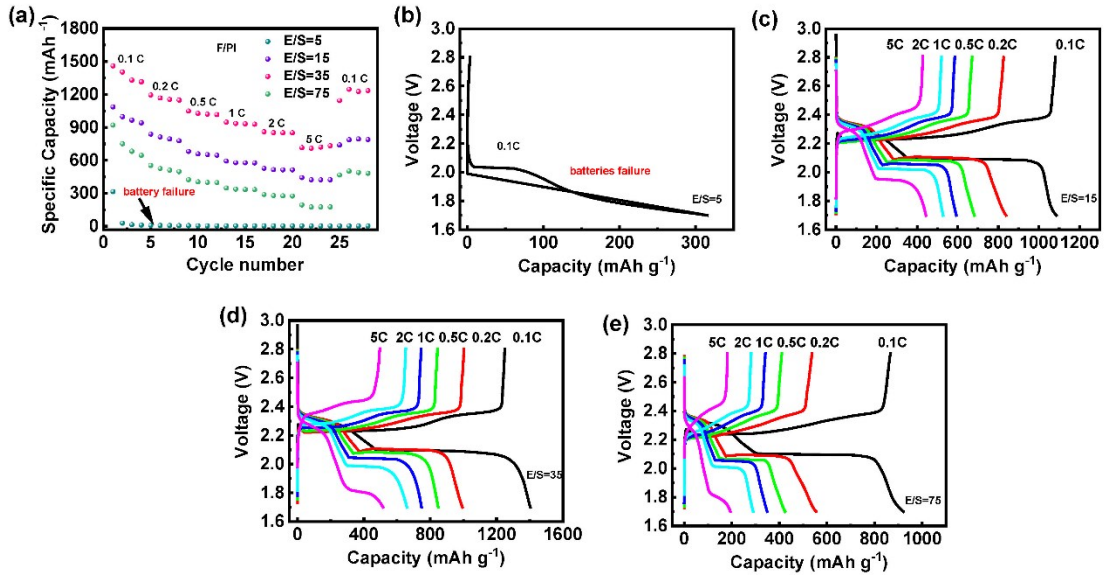

Fig. S12. (a) Rate capability and (b-e) discharge-charge profiles of the battery assembled by F/PI separators with E/S (electrolyte/sulfur, unit: μL/mg) ratio of 5, 15, 35, and 75, respectively.

Note: the mass loading of per battery is around 1.5~1.8 mg, thus the electrolyte amount is around 7.5~9.0, 22.5~27.0, 67.5~81.0, 112.5~135 μL with E/S ratio of 5, 15, 35, and 75, respectively. Due to the free-standing and porous property of F/PI separators, the electrolyte amount is much higher than those with Celgard batteries. When the E/S ratio is ultralow at 5, the F/PI batteries cannot be wet completely, and thus we observed batteries failure in Fig. S12a, b. The capacity is optimized to 1010 mAh g^{-1} at 0.2 C when the E/S ratio is around 35, which is 170 and 430 mA h g^{-1} higher than those with E/S ratio of 15 and 75, respectively (Fig. S12c-e). Because too much electrolyte leads to severe LiPS shuttling effect and thus the capacity decreases (Fig. S12e). Thus, in this manscript, we choose 70 μL of electrolyte (E/S=35) as the testing amount.

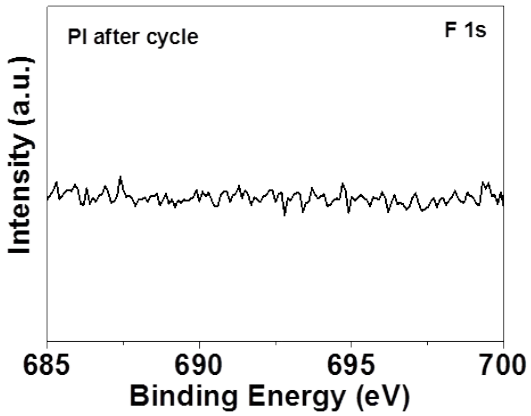

Fig. S13. XPS of F 1s peaks for PI separator after cycling tests.

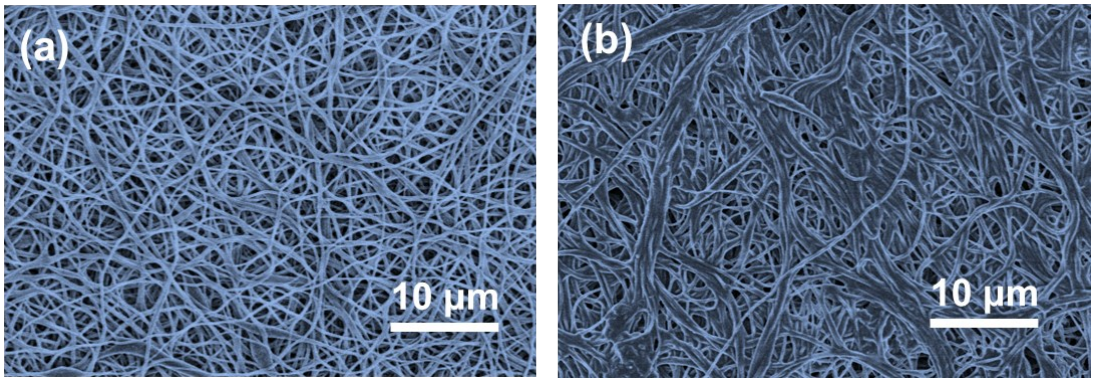

Fig. S14. SEM for (a) F/PI and (b) PI nanofiber membrane after discharge-charge for 200 cycles

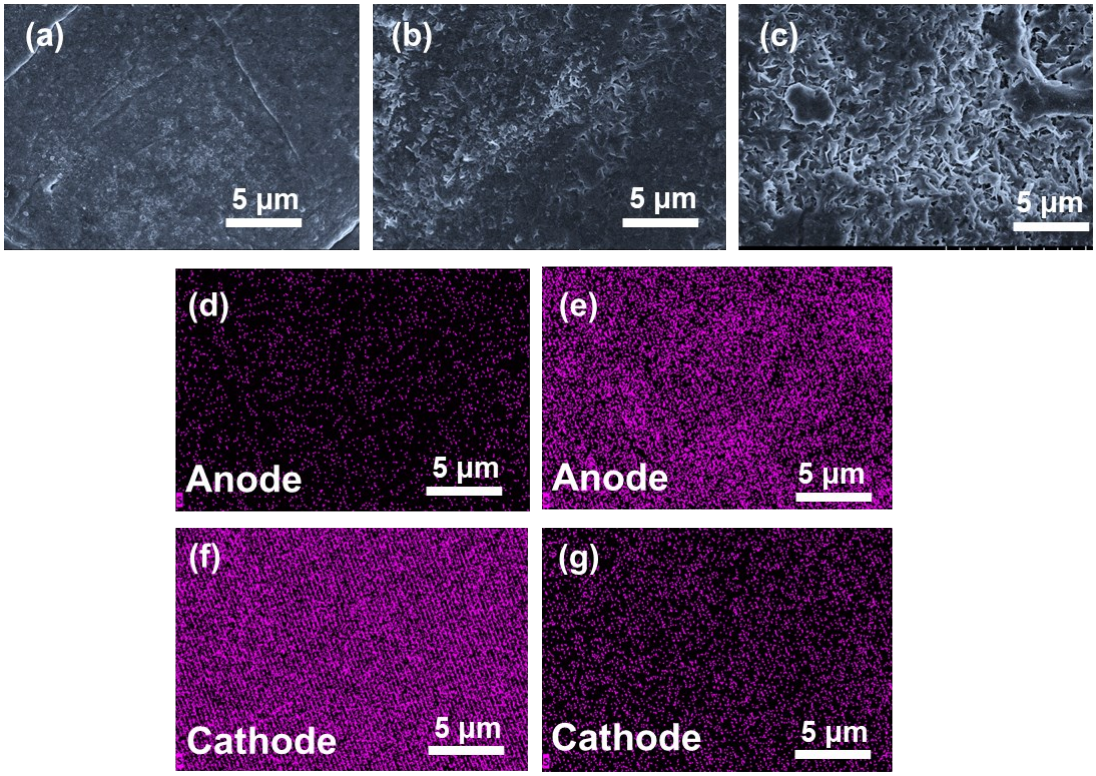

Fig. S15. SEM images of the lithium anode (a) before and after rate performance with (b) F/PI and (c) Celgard separators, respectively. The corresponding elemental mappings of sulfur in the lithium anode with (d) F/PI and (e) Celgard separators after the rate tests, respectively. The corresponding elemental mappings of sulfur in cathode with (f) F/PI and (g) Celgard separators after the rate tests.

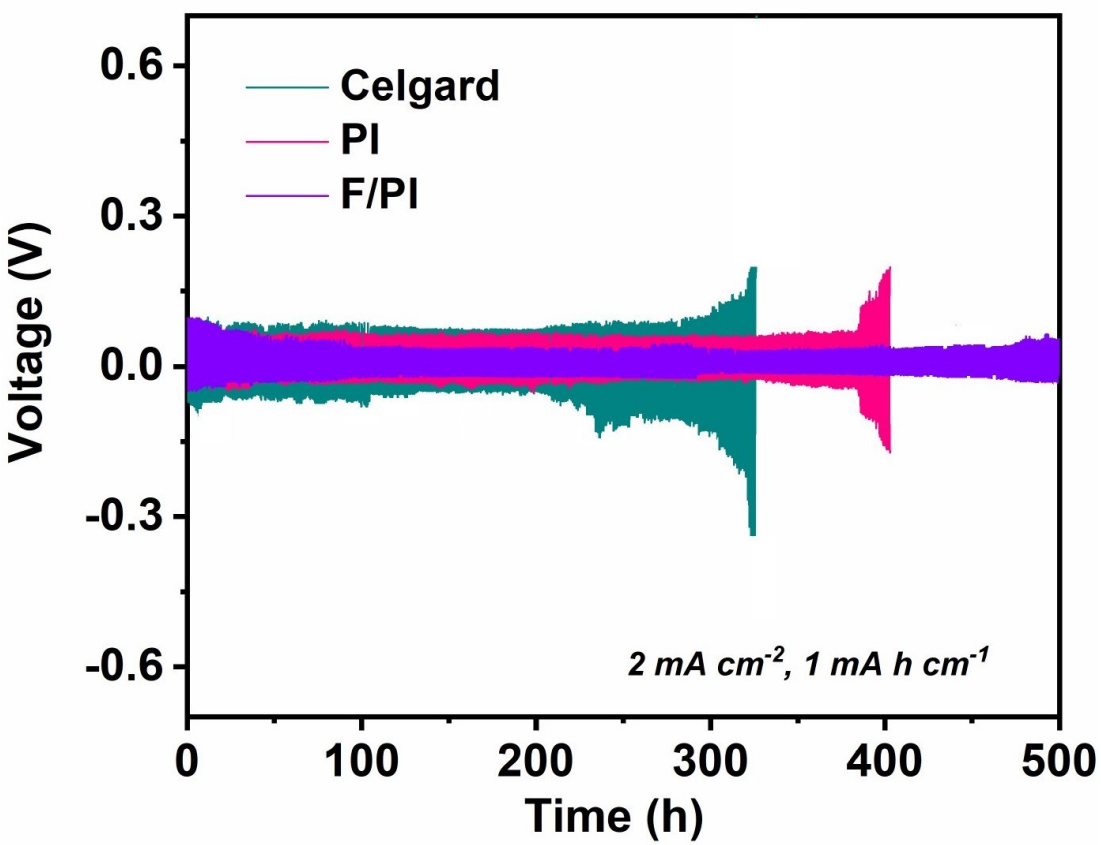

Fig. S16. Comparison of the cycling stability of Li plating/stripping stability with different separators at a current density of 2 mA cm^{-2} with a capacity limitation of 1 mA h cm^{-2}.

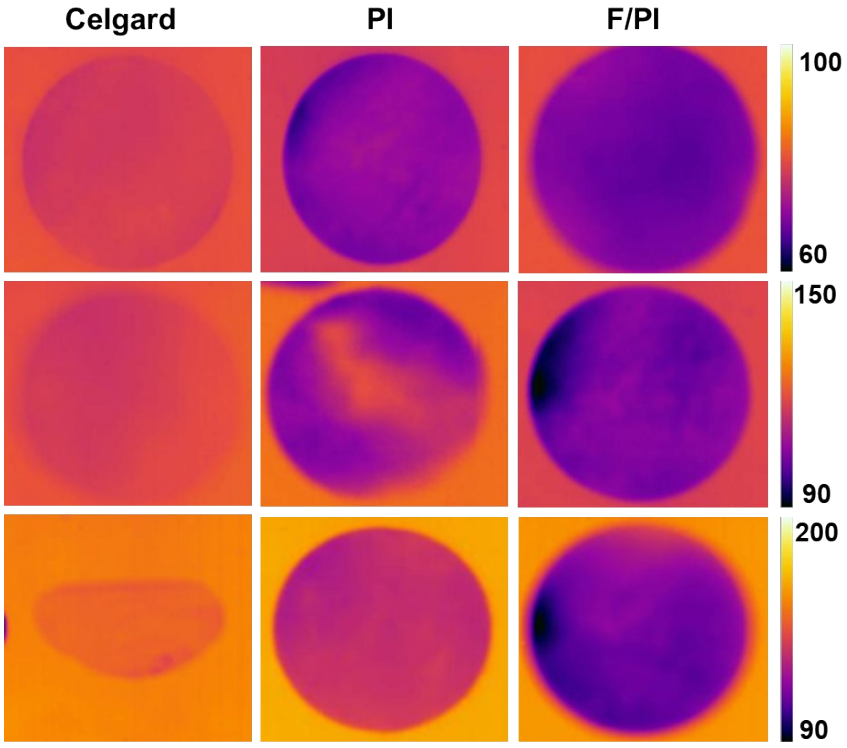

Fig. S17. Average thermograms of F/PI, PI, and Celgard separators.

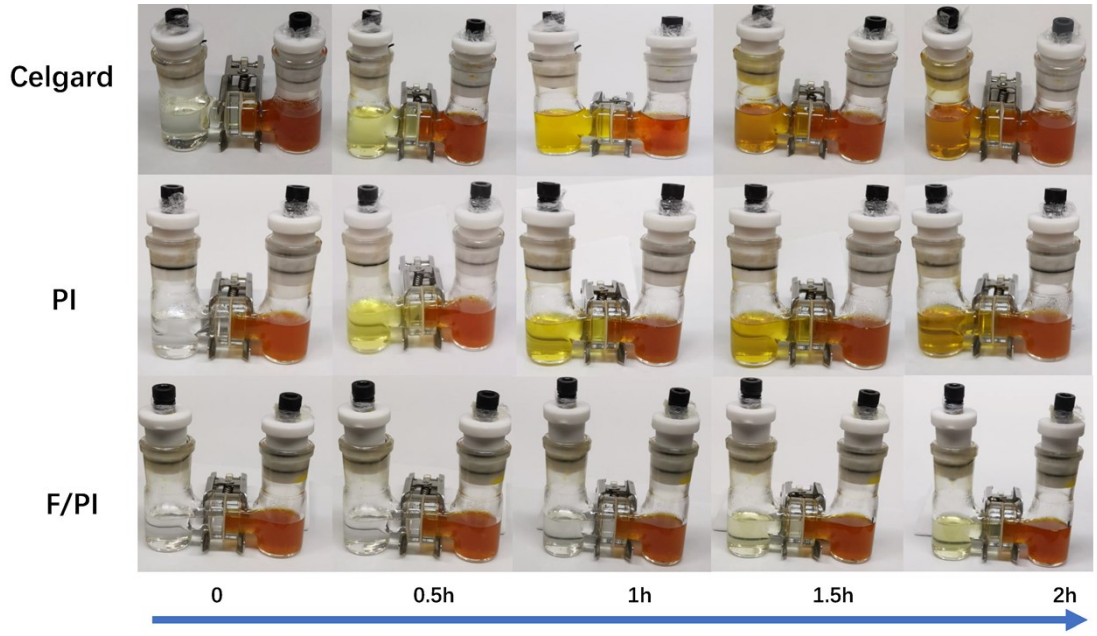

Fig. S18. Photographs comparison of polysulfide diffusion through the F/PI, PI and Celgard separators at 60°C.

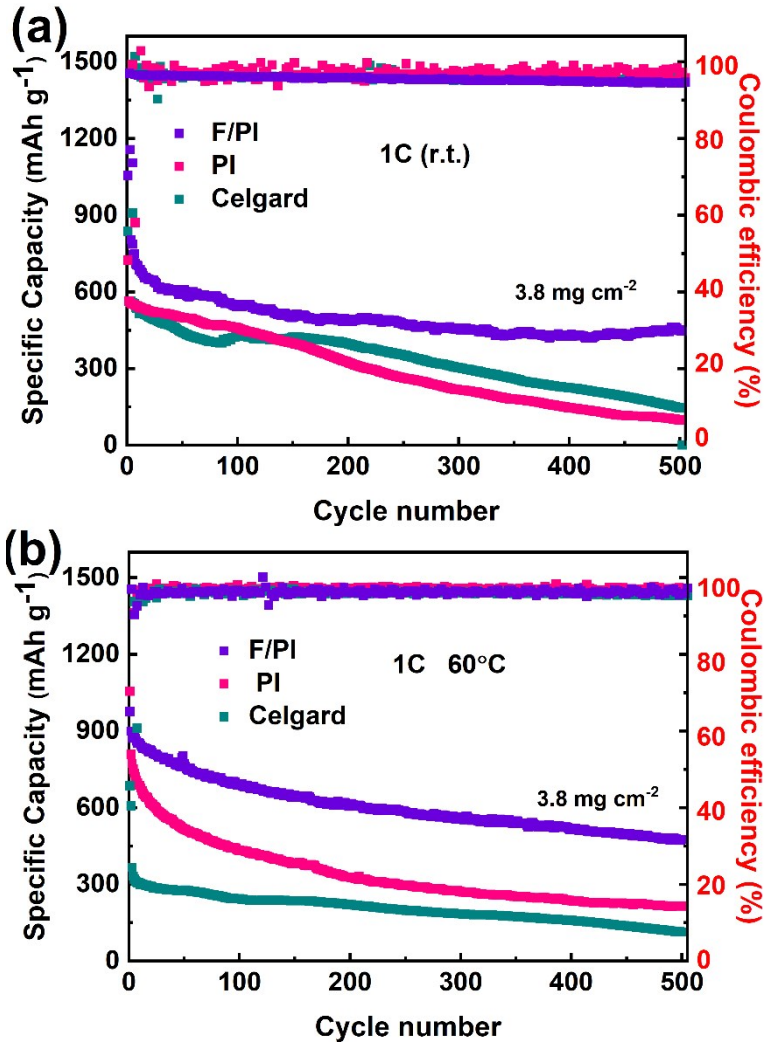

Fig. S19. Cycling performance of F/PI, PI, and Celgard-based batteries with higher sulfur loading at room temperature and high temperature (60°C).

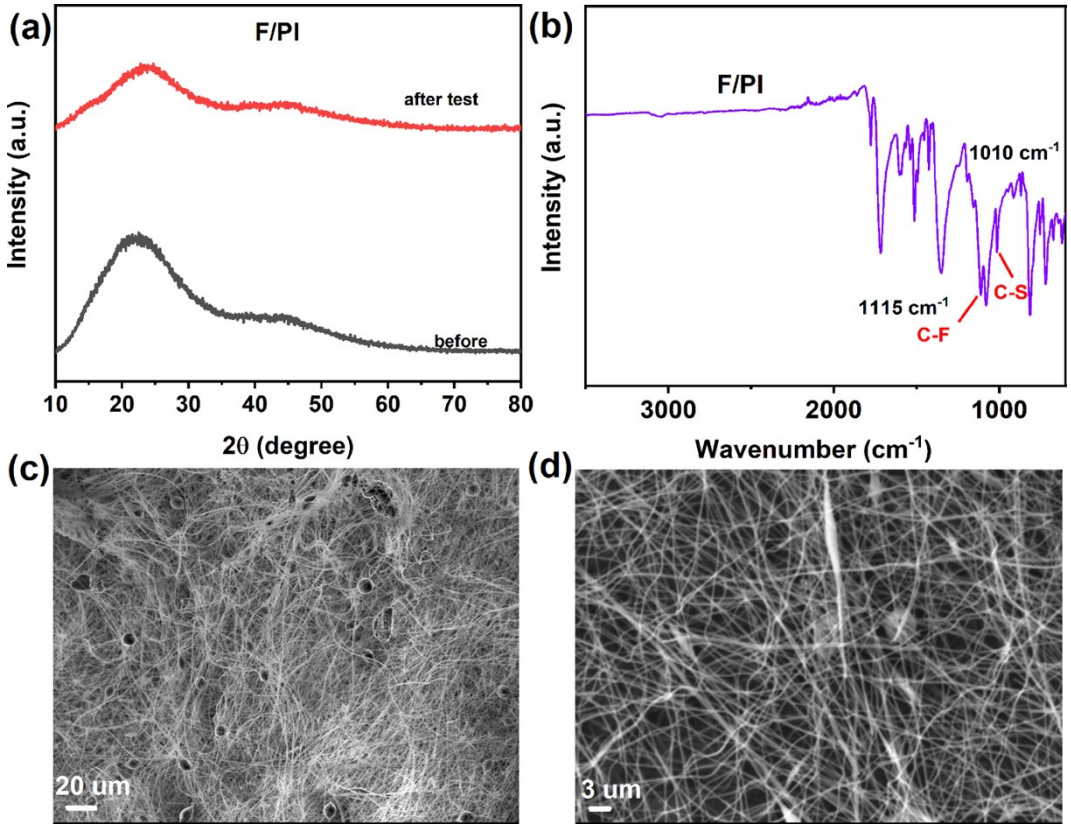

Fig. S20. (a) XRD patterns, (b) FT-IR spectra, (c, d) SEM images of F/PI separators after cycling performance at 60°C.

Table S1. Physical properties of F/PI, PI and Celgard separators.

Membrane	Thickness (μm)	Porosity (%)	Contact angle (º)	Electrolyte uptake (%)	Electrolyte retention (%)	Density (g cm^{-3})	Electronegativity (eV)
F/PI	30 ± 1.5	92.8 ± 0.5	0	2611	72	0.16	-4.7
PI	30 ± 1.5	92.1 ± 0.5	0	2011	58	0.15	-2.5
Celgard	25 ± 0.5	41.6 ± 0.8	53.5 ± 0.5	212	15	0.62	-

Table S2. Summary of lithium ion diffusion coefficients for F/PI, PI, and Celgard separators.

Parameters	Celgard	PI	F/PI
D_{Li^+} at peak O_1	1.14×10^{-14}	2.89×10^{-14}	5.12×10^{-14}
D_{Li^+} at peak R_1	1.25×10^{-15}	1.12×10^{-14}	1.25×10^{-14}
D_{Li^+} at peak R_2	1.99×10^{-15}	5.45×10^{-15}	7.93×10^{-15}

Table S3. Comparison of electrochemical performance of this work with previous excellent works involving new separators using carbon-sulfur cathodes in Li-S batteries

Separator	Sulfur loading (mg cm^{-2})	Initial capacity [mA h g^{-1}] (Current rate)	Rate capability [mA h g^{-1}] (Cycling rate)	Capacity retention [%] (Cycle number, Cycling rate)	Refs
PAN@APP [a]	1.8	780 (1C)	507 (3 C)	80.5% (400, 1 C)	[1]
MoO_3@CNT-PP	1.0	1425 (0.3 C)	655 (3 C)	53.0% (200, 0.3 C)	[2]
PP-C-St-TA	0.5	1500 (0.5 C)	600 (1 C)	57.7% (400, 0.5 C)	[3]
LNS/CB-Celgard	1.0-1.2	881(1C)	758 (2 C)	85.8% (500, 1 C)	[4]
PNG	1.0	1135 (0.5 C)	988 (2 C)	70.3% (300, 0.5 C)	[5]
LSB-LiSPEEK	2.4	1227 (0.2 C)	598 (2 C)	76.4% (100, 0.2 C)	[6]
$(M–P/P)_{10}$	1.2	1050 (0.5 C)	766 (3 C)	76.2% (100, 0.5 C)	[7]
MoS_2/Celgard	--	808 (0.5 C)	800 (1 C)	49.6% (600, 0.5C)	[8]
PAA	2.2	1459 (0.1 C)	408 (5 C)	76.1% (200, 0.2C)	[9]
MXene/ESM	2.7	1100 (0.5 C)	680 (1 C)	52.0% (250, 0.5 C)	[10]
F/PI	**1.5-1.8**	**1512 (0.1 C)**	**528 (5 C)**	**95.6% (500, 1 C)**	**This work**

[a] PAN@APP: Polyacrylonitrile (PAN) and ammonium polyphosphate

[b] MoO_3@CNT-PP: MoO_3 and carbon nanotubes-Celgard

[c] PP-C-St-TA: Celgard-styrene-tertiary amine

[d] LNS/CB-Celgard: laponite nanosheets/carbon black coated Celgard

[e] PNG: Porphyrinderived graphene-based nanosheets

[f] LiSPEEK: Lithiated sulfonated poly(ether ether ketone)

[g] M–P/P: MoS_2/poly(diallyl dimethyl ammonium chloride)/poly(acrylic

[h] PAA: Polyamic acid

[i] ESM: Eggshell membrane

Reference

[1] T. Y. Lei, W. Chen, Y. Hu, W. Q. Lv, X. X. Lv, Y. C. Yan, J. W. Huang, Y. Jiao, J. W. Chu, C. Y. Yan, C. Y. Wu, Q. Li, W. D. He and J. Xiong, *Adv. Energy Mater.,* 2018, **8**, 1802441.

[2] L. Y. Luo, X. Y. Qin, J. X. Wu, G. M. Liang, Q. Li, M. Liu, F. Y. Kang, G. H. Chen and B. H. Li, *J. Mater. Chem. A,* 2018, **6**, 8612.

[3] Q. Dong, R. P. Shen, C. P. Li, R. Y. Gan, X. Y. Ma, J. C. Wang, J. Li and Z. D. Wei, *Small,* 2018, **14**, 1804277.

[4] Y. F. Yang and J. P. Zhang, *Adv. Energy Mater.* 2018, **8**, 1801778.

[5] L. Kong, B. Q. Li, H. J. Peng, R. Zhang, J. Xie, J. Q. Huang and Q. Zhang, *Adv. Energy Mater.,* 2018, **8**, 1800849.

[6] Z. Li, Y. Han, J. H. Wei, W. Q. Wang, T. T. Cao, S. M. Xu and Z. H. Xu, *ACS Appl. Mater. Interfaces,* 2017, **9**, 44776.

[7] Z. A. Ghazi, X. He, A. M. Khattak, N. A. Khan, B. Liang, A. Iqbal, J. X. Wang, H. Sin, L. S. Li and Z. Y. Tang, *Adv. Mater.,* 2017, **29**, 1606817.

[8] J. Y. Wu, H. X. Zeng, X. W. Li, X. Xiang, Y. G. Liao, Z. G. Xue, Y. S. Ye and X. L. Xie, *Adv. Energy Mater.* 2018, **8**, 1802430.

[9] X. Luo, X. B. Lu, G. Y. Zhou, X. Y. Zhao, Y. Ouyang, X. B. Zhu, Y. E. Miao, T. X. Liu, *ACS Appl. Mater. Interfaces,* 2018, **10**, 42198.

[10] L. X. Yin, G. Y. Xu, P. Nie, H. Dou and X. G. Zhang, *Chem. Eng. J.,* 2018, **352**, 695.